

# Inferring 3D Object Pose in RGB-D Images

Saurabh Gupta

UC Berkeley

[sgupta@eecs.berkeley.edu](mailto:sgupta@eecs.berkeley.edu)

Ross Girshick  
Microsoft Research

[rbg@microsoft.com](mailto:rbg@microsoft.com)

Pablo Arbeláez

Universidad de los Andes, Colombia

[pa.arbelaez@uniandes.edu.co](mailto:pa.arbelaez@uniandes.edu.co)

Jitendra Malik  
UC Berkeley

[malik@eecs.berkeley.edu](mailto:malik@eecs.berkeley.edu)

## Abstract

The goal of this work is to replace objects in an RGB-D scene with corresponding 3D models from a library. We approach this problem by first detecting and segmenting object instances in the scene using the approach from Gupta et al. [13]. We use a convolutional neural network (CNN) to predict the pose of the object. This CNN is trained using pixel normals in images containing rendered synthetic objects. When tested on real data, it outperforms alternative algorithms trained on real data. We then use this coarse pose estimate along with the inferred pixel support to align a small number of prototypical models to the data, and place the model that fits the best into the scene. We observe a 48% relative improvement in performance at the task of 3D detection over the current state-of-the-art [33], while being an order of magnitude faster at the same time.

## 1. Introduction

Consider Figure 1. Understanding such an indoor image ultimately requires replacing all the objects present in the scene by three dimensional models. Traditionally, computer vision researchers have studied the problems of object detection, semantic and instance segmentation, fine-grained categorization and pose estimation. However, none of those outputs by itself is enough for, *e.g.*, a robot to interact with this cluttered environment. This work strives to achieve such a level of scene understanding in RGB-D images.

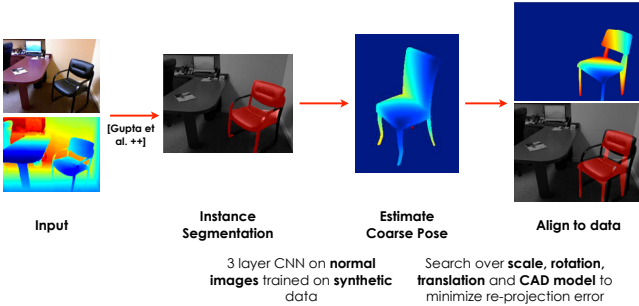
The output of our proposed system is visualized in Figure 1. Our approach is able to successfully retrieve relevant models and align them with the data. Such an output does not only address traditional problems of detection, segmentation, pose estimation and fine-grained recognition, but it goes beyond. The explicit correspondence with a 3D CAD model allows a representation which, from a robotics per-



Figure 1: **Output of our system:** Input RGB-D image and output a 3D model associated with objects in the scene.

spective, can be used directly for trajectory optimization, motion planning, and grasp estimation among other tasks. In this setting, a coarse output such as a bounding box at 50% overlap around the instance, or a segmentation mask marking pixels belonging to the object, or a fine-grained distinction between an office chair and a dinning room table, or a coarse viewpoint estimate of front facing versus side facing are insufficient.

Figure 2 describes the pipeline of our approach. We first use the output of the state-of-the-art detection and segmentation system [13], and infer the pose of the object using a neural network. We train this CNN on synthetic data and use normal images instead of depth images as input. We show that this CNN trained on synthetic data works better than the one trained on real data. We then use the top two inferred pose hypothesis to initialize a search over a small set of 3D model, their scales and exact placement. We use iterative closest point (ICP) for doing this and show that when initialized properly this works well even when working at the level of object categories rather than exact instances for which ICP has traditionally been used. In doing so we only use 2D annotations on the image and are able to generate



**Figure 2: Overview of approach:** We start with object detection and instance segmentation output from Gupta *et al.* [13]. We first infer the pose of the object using a convolutional neural network, and then search for the best fitting model that explains the data.

a 3D representation of the scene richer than one that was annotated.

Our final output is a 3D model that has been aligned to the objects present in the image. The richness and quality of the output from our system is illustrated when we compare to current state-of-the-art methods for 3D detection. A natural side-product of our output is a 3D bounding box for each object in the scene. When we use this 3D bounding box for 3D detection we observe that we are able to outperform the current state-of-the-art method [33] by 19% absolute AP points (48% relative), while at the same time being at least an order of magnitude faster.

## 2. Related Work

A large body of work in computer vision has focused on the problem of object detection, where the final output is a bounding box around the object, overlapping with the actual extent of the object by more than 50% [7, 37, 6, 8, 25]. There has also been substantial work on labeling each pixel in the image with a semantic label *e.g.* [5, 1]. Recent work from Hariharan *et al.* [14], Tighe *et al.* [36] brings these two lines of work together by inferring the pixel support of object instances.

There have been corresponding works for RGB-D images studying the problem of object detection [17, 34, 20, 21, 35, 13, 33, 19, 23, 4], semantic segmentation [3, 12, 18, 24, 31, 13, 32], and more recently instance segmentation [13, 32]. Since our approach builds on an object detection system, we discuss this body of research in more detail. [11, 17, 34, 35] propose modification to deformable part models [7] to adapt them to the RGB-D domain. Gupta *et al.* [13] also reason in the 2D image space and propose a geocentric embedding for depth images into horizontal disparity, height above ground and angle with gravity to learn features on bottom-up bounding box proposals using

a CNN. They also produce an instance segmentation where they label pixels belonging to the object for each detection. [23] also operate in a similar paradigm of reasoning with bottom-up region proposals, but focus on modeling object-object and object-scene context.

We note that, although all of these outputs are useful representations, but each of them is far from an understanding of the world that would enable a robot to interact with it.

Of course we are not the first one to raise this argument. There has been a lot of research on 3D scene understanding from a single RGB image [15, 28], and 3D object analysis [22, 2, 16, 39, 29]. Given the challenging nature of the problem, most of these works either study unoccluded clean instances, or fail under clutter. In this paper, we study the problem in the context of the challenging NYUD2 dataset and analyze how RGB-D data can be effectively leveraged for this task.

The most relevant research to our work comes from Song and Xiao [33] and Guo and Hoiem [10]. Song and Xiao [33] reason in 3D and train exemplar SVMs using synthetic data and slide these exemplars in 3D space to search for objects thus naturally dealing with occlusion, and study the tasks of both 2D and 3D detection. Their approach is inspiring but computationally expensive (25 minutes per image per category). [33] also show examples where their model is able to place a good fitting exemplar to data, but they do not empirically study the problem of estimating good 3D models that fit the data. We differ from their philosophy and propose to do 2D reasoning to effectively prune out large parts of the search space, and then do detailed 3D reasoning with the top few winning candidates. As a result, our final system is significantly faster (taking about two minutes per image). We also show that lifting from a 2D representation to a 3D representation is possible and show that naively fitting a box around the detected region outperforms the model from [33].

Guo and Hoiem [10] start with a bottom-up segmentation, retrieve nearest neighbors from the training set, and align the retrieved candidate with the data. In contrast, we use category knowledge in the form of top-down object detectors and inform the search procedure about the orientation of the object. Moreover, our algorithm does not rely on detailed annotations (which take about 5 minutes for each scene) [9] of the form used in [10]. We also propose a category-level metric to evaluate the rich and detailed output from such algorithms. Finally, [27, 30] among many others, work on the same problem but either consider known instances of objects, or rely on user interaction.

## 3. Estimating Coarse Pose

In this section, we propose a convolutional neural network to estimate the coarse pose of rigid objects from a depth image.

We first observe that reliable annotations for such a detailed task are extremely challenging to obtain [9]. At the same time, a large amount of synthetic data can be obtained by rendering a library of 3D models in different poses. Thus, it is desirable to be able to train the algorithm on synthetic data instead of real data.

Secondly, the representation of the input is important. Gupta *et al.* [13] proposed an HHA embedding for a depth image for feature learning in a CNN, and demonstrated that this embedding is superior to just using the depth image by itself. We observe that, while this embedding is appropriate for detecting objects (a chair is defined by a horizontal surface at some height), it effectively removes critical information about the pose of the object. As an example, consider a chair rotating about the vertical axis. As the chair rotates, its pose changes, but both its height above ground and its angle with gravity remain fairly constant. It is therefore important to choose an appropriate depth embedding for the task we address.

Thirdly, occlusion is a predominant phenomenon in indoor environments (consider for instance chairs in a conference room). It will be desirable for an algorithm for pose estimation to be robust to occlusion where parts of the object may not be visible.

Lastly, depth images have more regularities than color images (because of the absence of texture), and we want to generalize from synthetic data to real data, hence the network should not have a very large capacity.

With these motivations in mind, we propose to learn our coarse pose estimator from synthetic data which consists of aligned 3D CAD models for different categories.

Assume  $C(k, n, s)$  is a convolutional layer with kernel size  $k \times k$ ,  $n$  filters and a stride of  $s$ ,  $P_{\{\max, \text{ave}\}}(k, s)$  a max or average pooling layer of kernel size  $k \times k$  and stride  $s$ ,  $N$  a local response normalization layer,  $RL$  a rectified linear unit, and  $D(r)$  a dropout layer with dropout ratio  $r$ . Our network has the following architecture:  $C(7, 96, 4) - RL - P_{\max}(3, 2) - D(0.5) - N - C(5, 128, 2) - RL - P_{\max}(3, 2) - N - C(3, |(N_{\text{pose}} + 1)N_{\text{class}}|, 1) - RL - P_{\text{ave}}(14, 1)$

We chose a smaller fully convolutional network to account for the fact that depth images have more regularities. In the same vein, the classification layer at the end is an average pooling over the neurons of the previous layer. We deliberately did not use fully connected layers and introduced a dropout layer after *conv1* in order to make the network robust to occlusion.

We observe that the HHA encoding proposed in [13] explicitly removes the azimuth direction by considering only the disparity, angle with gravity and height above ground. Thus, we propose to use the normal image as input to the network. We use 3 channel normal images where the three channels encode  $N_x$ ,  $N_y$  and  $N_z$  as the angle the normal

vector makes with the three geocentric directions estimated using the algorithm from [12]. We scale this to be in degrees and shift it to center at 128 instead of 90.

We train this network for classification using a soft-max loss and share the lower layers of the network among different categories. We also adopt the geocentric constraint and assume that the object rests on a surface and hence must be placed flat on the ground. Thus, we only have to determine the azimuth of the object in the geocentric coordinate frame. We bin this azimuth into  $N_{\text{posebin}}$  bins and train the network to predict the bin for each example.

We use 3D models from ModelNet [38] to train the network. In particular, we use the subset of models as part of the training set and work with the 10 categories for which the models from each category are aligned to have a canonical pose (bathtub, bed, chair, desk, dresser, monitor, nightstand, sofa, table, toilet). We sample 50 models for each category and render 10 different poses for each model placed on a horizontal floor at locations and scales as estimated from the NYUD2 dataset [31]. We place one object per scene, and sample boxes with more than 70% overlap with the ground truth box as training examples. We crop and warp the bounding box in the same way as Girshick *et al.* [8]. Note that warping the normals preserves the angles that are represented (as opposed to warping a depth image or a HHA image [13] which will change the orientation of surfaces being represented).

At test time, we simply forward propagate the image through the network and take the output pose bin as the predicted pose estimate. Given that the following stage requires a good initialization, we work with the top  $k (= 2)$  modes of prediction, rather than a single prediction.

## 4. Model Alignment

In this section we describe how we place the object in the scene. We start from the instance segmentation output from [13], and infer the coarse pose of the object using the neural network introduced in Section 3. With this rough estimate of the pixel support of the object and a coarse estimate of its pose, we solve an alignment problem to obtain an optimal placement for the object in the scene.

### 4.1. Model Search

Note that our pose estimator only gives us an orientation for the model. It does not inform about the size of the object, or about which model would fit the object best. Thus this stage has to search over scale and models and infer the exact rotation  $R$  and translation  $t$  that aligns the model best with the data. We search over scale and models, optimizing for a rotation  $R$  and a translation  $t$  that best explain the data.

To search over scale, we gather category level statistics from the 3D bounding box annotations from [9]. In particular, we use the area of the bounding box in the top view, and

estimate the mean of this area and its standard deviation, and take  $N_{scale}$  stratified samples from  $\mathcal{N}(\mu_{area}, \sigma_{area})$ . Such statistics do not require annotations and can also be obtained from online furniture catalogues. To search over scale, we isotropically scale each model to have this area in the top-view.

To search over models, we manually pick a small number  $N_{models}$  (about 5) of 3D models for each category. Care was taken to pick distinct models, but this could also be done in a data-driven manner (by picking models which explain better the data at hand).

Finally, we optimize over  $R$  and  $t$ . We do this iteratively using iterative closest point (ICP) [26], which we modify by constraining the rotation estimate to be consistent with the gravity direction. We initialize  $R$  using the pose estimate obtained from Section 3, and the inferred direction of gravity [12]. We initialize translation  $t$  by using the median of the world co-ordinates of the points in the segmentation mask, to set  $t_x$  and  $t_z$ , and set  $t_y$  such that the model is resting on the floor. (This constraint helps with heavily occluded objects *e.g.* chairs for which often only the back is visible). The following subsection describes the model alignment procedure.

## 4.2. Model Alignment

The input to the model alignment algorithm is a depth image  $D$ , a segmentation mask  $S$ , a 3D model  $M$  at a given fixed scale  $s$  and an initial estimate of the transformation (a rotation matrix  $R_0$  and a translation vector  $t_0$ ) for the model. The output of the algorithm is a rotation  $R$  and a transformation  $t$ , such that the 3D model  $M$  rendered with transformations  $R$  and  $t$  explains as many points as possible in the segmentation mask  $S$ . We solve this problem approximately by the following procedure which we repeat for  $N$  iterations.

- 1. Render model:** Use the current estimate of the transformation parameters ( $s, R, t$ ) to render the model  $M$  to obtain a depth image of the model. Project points from the depth image that belong to the segmentation mask  $S$ , and the points from the rendered model’s depth image to 3D space, to obtain two point sets  $P_{object}$  and  $P_{model}$ .
- 2. Re-estimate model transformation parameters:** Run ICP to align points in  $P_{object}$  to points in  $P_{model}$ . We form correspondence by associating each point in  $P_{object}$  with the closest point in  $P_{model}$ , which prevents associations for occluded points in the object. We also reject the worst 20% of the matches based on the distance. This allows the association to be robust in the presence of over-shoot in the segmentation mask  $S$ . Lastly, while estimating the updates of the transformation ( $R, t$ ), we enforce an additional constraint that

the rotation matrix  $R$  must rotate the object only about the direction of gravity.

## 4.3. Model Selection

Now we need to select the fitted model that best explains the data among  $N_{scale}N_{model}$  candidates. We pose this selection as a learning problem and compute a set of features to capture the quality of the fit to the data. We compute the following features: number and fraction of pixels of the rendered model that are occluded, which are explained by the data, fraction and number of pixels of the input instance segmentation which are explained by the model, intersection over union overlap of the instance segmentation with mask of the model explained by the data, and mask of the model which is unoccluded. We learn a linear classifier on these features to pick the best fitting model. This classifier is trained with positives coming from rendered models which have more than 50% overlap with a ground truth region.

## 5. Experiments

We evaluate our approach on the NYUD2 dataset from Silberman *et al.* [31] and use the standard train set of 795 images and test set with 654 images. We split the 795 training images into 381 train and 414 validation images. For synthetic data we use the collection of aligned models made available by Wu *et al.* [38].

### 5.1. Coarse Pose Estimation

Here we describe our experiments to evaluate our coarse pose estimator. We present two evaluations, one on synthetic data and another one on real data.

**Measuring Performance** To measure performance, we work with ground truth boxes, and consider the distribution of the angular error in the top view. In particular, we plot the angular error  $\delta_\theta$  on the X-axis and the accuracy (the fraction of data which incurs less than  $\delta_\theta$  error) on the Y-axis. Note that we plot this graph for small ranges of  $\delta_\theta$  ( $0^\circ$  to  $45^\circ$ ) as accuracy in the high error ranges is useless from the perspective of our model alignment, where an initialization very far from the actual pose often fails to align well. What is more desirable is a high  $\text{top}_k$  accuracy (fraction of instances which are within  $\delta_\theta$  of the  $\text{top}_k$  predictions of the model). The rationale is that the model alignment step can use multiple hypothesis and pick the best among them.

**Evaluating on synthetic data** Figure 3 shows the performance on the synthetic data. This synthetic testing data is obtained the same way as the synthetic training data, except that it comes from a distinct set of models as compared to the training set. We experimented with the number of models in the training set and looking at the error when consid-

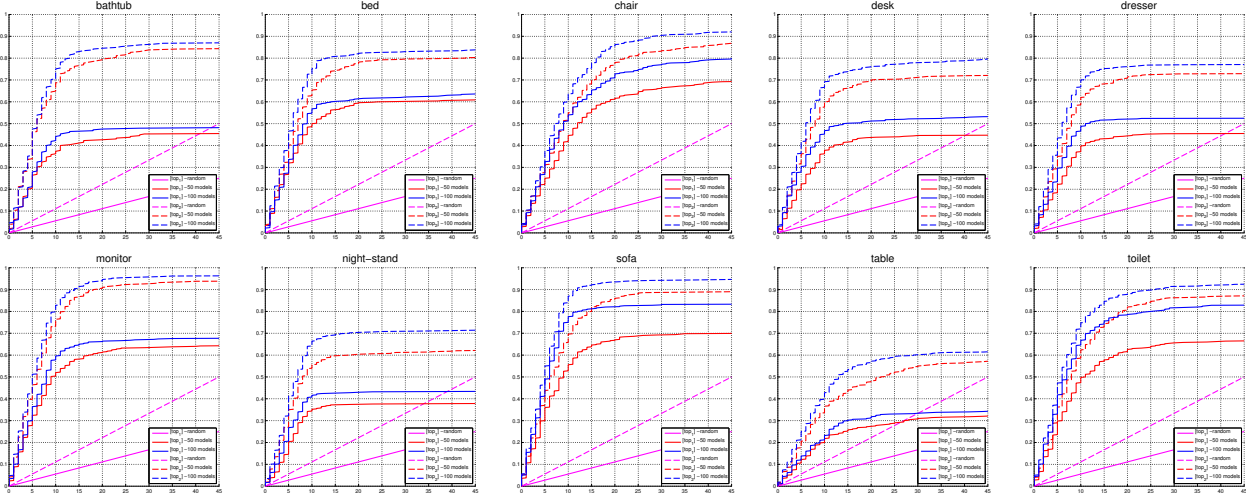


Figure 3: Performance on a synthetic test set. We plot accuracy (fraction of instances for which we are able to predict pose within a  $\delta_\theta$  angle) as a function of  $\delta_\theta$ . We experiment with using 50 or 100 models for each category for training, and also look at how the performance changes when using best of  $top_1$  or  $top_2$  modes of the output.

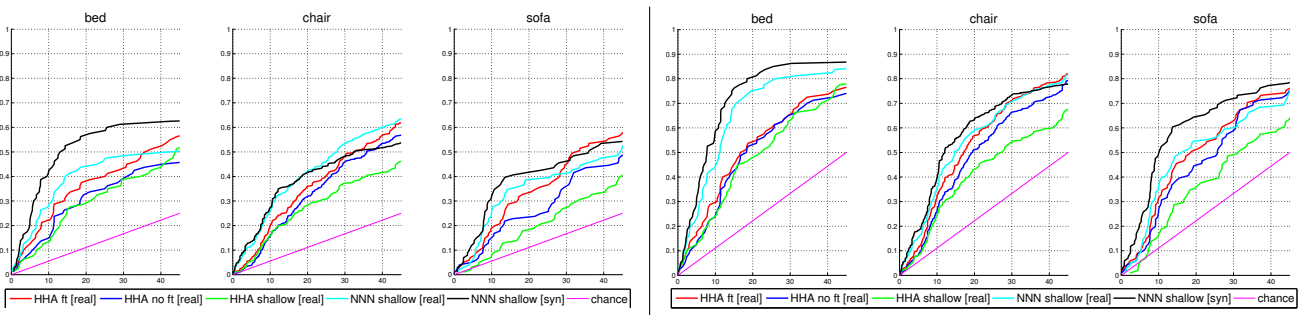


Figure 4: Performance on a real val set. We plot accuracy (fraction of instances for which we are able to predict pose within a  $\delta_\theta$  angle) as a function of  $\delta_\theta$ . The left three plots show  $top_1$  accuracy and the right three plots  $top_2$  accuracy. Note that real in the legend refers to model trained on real data, syn refers to the model trained on synthetic data and NNN stands for normal image.

ering  $top_1$  and  $top_2$  pose estimates and see expected trends: more models help and that there is a large increase in recall when considering two hypothesis as opposed to one.

**Evaluating on real data** We now proceed to test our trained model on real data. Here we work with the annotations from Guo and Hoiem [9]. Guo and Hoiem annotate the NYUD2 dataset with 3D CAD models for the following 6 categories: chair, bed, sofa, table, desk and book shelf. To obtain interpretable results we work with categories which have a clearly defined pose: chair, sofa and bed (we would have liked to also work with bookshelf, but it is not among the 10 categories which are pose aligned in ModelNet [38]). In Figure 4 we plot the same curves as for synthetic data. The top row plots the  $top_1$  accuracy and the second row plots  $top_2$  accuracy. Note that there is a large number of

objects which have missing depth data (for instance 30% of chairs have more than 50% missing depth pixels), hence we plot these curves only for instances with less than 50% depth pixels missing. We compare against other algorithms. We experimented with the HHA network from [13] with and without fine-tuning for this task, training a shallow network from random initialization using HHA images and normal images. All these experiments are done by training on the real data, and we see that we are able to outperform these variants by training on clean synthetic data.

## 5.2. Model Fitting

An input to our model fitting procedure is an initial pixel support for the object to fit to the model. We first describe and evaluate the instance segmentation input we are using, describe how we can accurately lift 2D output to 3D. To

Table 1: **Test set results for detection and instance segmentation on NYUD2:** First line reports  $AP^b$  (bounding box detection  $AP$ ) performance using features from just the bounding box and second line reports  $AP^b$  when using features from the region mask in addition to features from the bounding box. Third and fourth lines report the corresponding performance when using the full trainval set to finetune (instead of only using the train set). Subsequent lines report  $AP^r$  (region detection  $AP$  [14]). Using features from the region in addition to features from the box (row 6) improves performance over the refinement method used in [13] (row 5). Finally, finetuning over the trainval set boosts performance further.

| task   |                        | finetuning set | mean        |             |             |             |            |             |             |             |             |             |             |             |             |             |             |             |             |             |             |             |
|--------|------------------------|----------------|-------------|-------------|-------------|-------------|------------|-------------|-------------|-------------|-------------|-------------|-------------|-------------|-------------|-------------|-------------|-------------|-------------|-------------|-------------|-------------|
|        |                        |                |             | bathub      | bed         | book shelf  | box        | chair       | counter     | desk        | door        | dresser     | garbage bin | lamp        | monitor     | night stand | pillow      | sink        | sofa        | table       | television  | toilet      |
| $AP^b$ | [13]                   | train          | 35.9        | 39.5        | 69.4        | 32.8        | 1.3        | 41.9        | 44.3        | 13.3        | 21.2        | 31.4        | 35.8        | 35.8        | 50.1        | 31.4        | 39.0        | 42.4        | 50.1        | 23.5        | 33.3        | 46.4        |
|        | [13] + Region Features | train          | 39.3        | <b>50.0</b> | 70.6        | 34.9        | 3.0        | 45.2        | <b>48.7</b> | <b>15.2</b> | 23.5        | 32.6        | 48.3        | 34.9        | 50.2        | 32.2        | <b>44.2</b> | 43.1        | <b>54.9</b> | 23.4        | 41.5        | 49.9        |
|        | [13]                   | trainval       | 38.8        | 36.4        | 70.8        | 35.1        | 3.6        | 47.3        | 46.8        | 14.9        | 23.3        | 38.6        | 43.9        | <b>37.6</b> | <b>52.7</b> | 40.7        | 42.4        | <b>43.5</b> | 51.6        | 22.0        | 38.0        | 47.7        |
|        | [13] + Region Features | trainval       | <b>41.2</b> | 39.4        | <b>73.6</b> | <b>38.4</b> | <b>5.9</b> | <b>50.1</b> | 47.3        | 14.6        | <b>24.4</b> | <b>42.9</b> | <b>51.5</b> | 36.2        | 52.1        | <b>41.5</b> | 42.9        | 42.6        | 54.6        | <b>25.4</b> | <b>48.6</b> | <b>50.2</b> |
| $AP^r$ | [13] (Random Forests)  | train          | 32.1        | 18.9        | <b>66.1</b> | 10.2        | 1.5        | 35.5        | 32.8        | <b>10.2</b> | <b>22.8</b> | 33.7        | 38.3        | <b>35.5</b> | 53.3        | <b>42.7</b> | 31.5        | 34.4        | 40.7        | 14.3        | 37.4        | 50.3        |
|        | [13] + Region Features | train          | 34.0        | 33.8        | 64.4        | 9.8         | 2.3        | 36.6        | 41.3        | 9.7         | 20.4        | 30.9        | 47.4        | 26.6        | 51.6        | 27.5        | <b>42.1</b> | 37.1        | 44.8        | 14.7        | 42.7        | 62.6        |
|        | [13] + Region Features | trainval       | <b>37.5</b> | <b>42.0</b> | 65.1        | <b>12.7</b> | <b>5.1</b> | <b>42.0</b> | <b>42.1</b> | 9.5         | 20.5        | <b>38.0</b> | <b>50.3</b> | 32.8        | <b>54.5</b> | 38.2        | 42.0        | <b>39.4</b> | <b>46.6</b> | <b>14.8</b> | <b>48.0</b> | <b>68.4</b> |

Table 2: **Test set results for 3D detection on NYUD2:** We report the 3D detection AP [33]. We use the evaluation code from [33]. ‘3D all’ refers to the setting with all object instances where as ‘3D clean’ refers to the setting when instances with heavy occlusion and missing depth are considered difficult and not used for evaluation [33]. See Section 5.2.2 for details.

| 3D all   |  |  |  |  |  |  |      |      |       |      |       |        |
|--|--|--|--|--|--|--|------|------|-------|------|-------|--------|
|  |  |  |  |  |  |  | mean | bed  | chair | sofa | table | toilet |
| Song and Xiao [33]   |  |  |  |  |  |  | 39.6 | 33.5 | 29.0  | 34.5 | 33.8  | 67.3   |
| Our (3D Box on instance segmentation from Gupta <i>et al.</i> [13])          |  |  |  |  |  |  | 48.4 | 74.7 | 18.6  | 50.3 | 28.6  | 69.7   |
| Our (3D Box around estimated model)  |  |  |  |  |  |  | 58.5 | 73.4 | 44.2  | 57.2 | 33.4  | 84.5   |
| Our [no RGB] (3D Box on instance segmentation from Gupta <i>et al.</i> [13]) |  |  |  |  |  |  | 46.5 | 71.0 | 18.2  | 49.6 | 30.4  | 63.4   |
| Our [no RGB] (3D Box around estimated model)                                 |  |  |  |  |  |  | 57.6 | 72.7 | 47.5  | 54.6 | 40.6  | 72.7   |

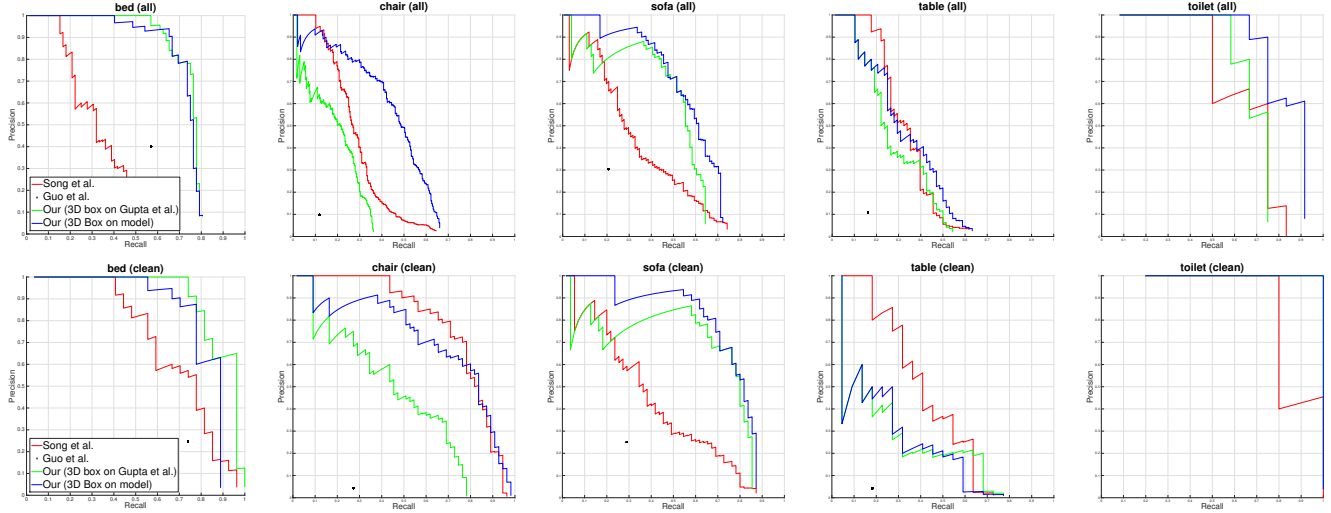
  

| 3D clean   |  |  |  |  |  |  |      |      |       |      |       |        |
|--|--|--|--|--|--|--|------|------|-------|------|-------|--------|
|  |  |  |  |  |  |  | mean | bed  | chair | sofa | table | toilet |
| Song and Xiao [33]   |  |  |  |  |  |  | 64.6 | 71.2 | 78.7  | 41.0 | 42.8  | 89.1   |
| Our (3D Box on instance segmentation from Gupta <i>et al.</i> [13])          |  |  |  |  |  |  | 66.1 | 90.9 | 45.9  | 68.2 | 25.5  | 100.0  |
| Our (3D Box around estimated model)  |  |  |  |  |  |  | 71.1 | 82.9 | 72.5  | 75.3 | 24.6  | 100.0  |
| Our [no RGB] (3D Box on instance segmentation from Gupta <i>et al.</i> [13]) |  |  |  |  |  |  | 62.3 | 86.9 | 43.6  | 57.4 | 26.6  | 96.7   |
| Our [no RGB] (3D Box around estimated model)                                 |  |  |  |  |  |  | 70.7 | 84.9 | 75.7  | 62.8 | 33.7  | 96.7   |

illustrate this we compare against [33] and [10] for the task of 3D detection [33]. Next, given the lack of metrics to evaluate 3D model placement, we describe a metric and the experiments that we used to make design choices for our model alignment algorithm. Finally, we show examples of our output.

### 5.2.1 Object Detection and Instance Segmentation

We note that the instance segmentation system proposed in [13] does not use the CNN to compute features on the bottom-up region but works with bounding boxes and later refines their support using a random forest. We experimented with features computed on the masked region in addition to features on the box as proposed by Hariharan *et al.* [14], and observe that these additional features im-



**Figure 5: Precision Recall Plots for 3D Detection:** Variation in  $AP^m$  as we change number of scales, number of models and number of pose hypothesis we search over in our model alignment stage.

prove performance for bounding box detection as well as instance segmentation, thus achieving state-of-the-art performance on these tasks (Table 1).  $AP^b$  goes up from 35.9% to 39.3%,  $AP^r$  improves from 32.1% [13] to 34.0%. Moreover, Gupta *et al.* [13] only finetuned the model on 381 training image,  $AP^b$  and  $AP^r$  both improve further when finetuning over the 795 trainval images (row 4 and row 7 in Table 1).

We work with these final instance segmentations for this work. Of course, one could refine these regions [13, 14] to obtain even better instance segmentations, but we chose to work with this output to minimize the number of times we train on the same data.

### 5.2.2 3D Detection

We next illustrate the richness of our approach by studying the task of 3D detection. Note that our method outputs a model aligned with objects in the image. A trivial side-product of our output is a 3D bounding box (obtained by putting a box around the inferred 3D model). We use this 3D bounding box as our output for the 3D detection task and compare to the method from Song and Xiao [33] which was specifically designed and trained for this task.

We study this task in the setting proposed by Song and Xiao in [33]. Song and Xiao work with the images from the NYUD2 dataset but create different splits for different categories and study two different tasks: a ‘clean’ task where they remove instances which are heavily occluded or have missing depth, and an ‘all’ task in which they consider all instances. Given they use non-standard splits which are different from the standard dataset splits that we use, we simply evaluate on the intersection of their test set for the cate-

gory and the standard test set for the dataset.

In addition we also compare to a simple baseline using the instance segmentation from [13] as described in Section 5.2.1 for 3D detection. We use a simple heuristic here: we put a tight fitting box around the 3D points in the inferred instance segmentation. We first determine the extent of the box in the top view by searching over the orientation of the rectangular box such that its area is minimized. We next set the bottom of the box to rest on the floor and estimate the height as the maximum height of the points in the instance segmentation. All these operations are done using percentiles ( $\delta$  and  $100 - \delta$ , with  $\delta = 2$ ) to be robust to outliers.

We report the performance in Table 2 and show the Precision Recall curves in Figure 5. We observe that this simple strategy of fitting a box around the inferred instance segmentation (denoted as ‘Our (3D Box on instance segmentation from Gupta *et al.* [13])’ in Table 2) already works better than the method proposed in [33] which was specifically designed for this task. At the same time, this method is fast (40 seconds CPU + 30 seconds on a GPU) and scales well with number of categories, as compared to 25 minutes per categories per image for [33]. This result illustrates that starting with efficient and well established 2D reasoning (since [13] does 2D reasoning they are more readily able to leverage rich features for RGB images) to prune out large parts of the search space is not only more efficient but also more accurate than 3D reasoning from the get go for such tasks.

Finally, a 3D box around our final output (denoted ‘Our (3D Box around estimated model)’) outperforms both [33] and the baseline of putting a 3D bounding box around the instance segmentation output, thus illustrating the efficacy

and utility of the methods proposed in the paper. There is a large improvement over the baseline in performance for non-box like objects, chair, sofa and toilet. The improvement for chair is particularly large (18.6% to 44.2% in the ‘all’ setting). This is because chairs are often heavily occluded (*e.g.* chair occluded behind a table) and the box around the visible extent is systematically an underestimate of the actual amodal box. We also note that our performance for tables is only comparable to [33]. This is because there is a mismatch between the definition of table as used by our object detectors (which are based on ground truth from [31, 13]) and ground truth used in the 3D detection benchmark from [33] (the mismatch comes from coffee-tables and desks being inconsistently marked as tables).

Guo and Hoiem [10] also aligns 3D CAD models to objects in the image. We also compare to their work on this 3D detection task. We take the scenes produced by the algorithm from [10], compute tight 3D bounding boxes around their detected objects and benchmark them in the same setup as described above to obtain a point on the Precision Recall plot as shown in Figure 5 for categories that both works study: bed, chair, table and sofa. This comparison is also largely favorable to our method.

Lastly, we also report performance of our system when only using the depth image for object detection, pose estimation and model placement steps (denoted ‘Our [no RGB] (3D Box on instance segmentation from Gupta et al. [13])’ and ‘Our [no RGB] (3D Box around estimated model)’) (the bottom-up region generation step still uses the RGB image, we do not expect this to impact this result significantly). It is interesting to see that this version of our system is better than the full version for some categories. We believe this is because RGB information allows our full system to detect objects with missing depth with high scores which go on to become high scoring false positives when the model placement step fails given the absence of enough depth data. On average this ablated version of our system performs comparably to our final system (57.6% versus 58.5% in the ‘3D all’ setting), and continues to outperform the algorithm from Song and Xiao [33]. This is consistent with the observation that  $AP^r$  for these two systems across these five categories is also fairly similar (mean  $AP^r$  without RGB features across these five categories: 44.5% compared to average  $AP^r$  full system: 47.4%).

### 5.2.3 Model Alignment Performance

**Measuring Performance** Given that the output of our algorithm is a 3D model placed in the scene, it is not immediately obvious how to evaluate performance. One might think of evaluating individual tasks such as pose estimation, sub-type classification, key point prediction or instance segmentation, but doing these independently does not measure

the performance of the task we are considering, which is beyond each of these individual tasks. Moreover, for many categories we are considering there may not be a consistent definition of pose (*e.g.* table), or key points (*e.g.* sofa), or sub-types (*e.g.* chair).

Thus, to surpass the limitation of these metrics to measure performance at our task of placing 3D models in the scene, we propose a new metric which directly evaluates the fit of the inferred model with the observed depth image. We assume that there is a fixed library of 3D models  $\mathcal{L}$ , and a given algorithm  $\mathcal{A}$  has to pick one of these models, and place it appropriately in the scene. We assume we have category level instance segmentations annotations for the categories we are studying.

Our proposed metric is a generalization of the Average Precision, the standard metric for evaluating detection and segmentation [14]. Instead of just using the image level intersection over union of the predicted box (in case of  $AP^b$ ) or region (in case of  $AP^r$ ) with the ground truth, we also enforce the constraint that the prediction must agree with the depth values observed in the image. In particular, we modify the way intersection between a prediction and a ground truth instance is computed. We render the model from the library  $\mathcal{L}$  as proposed by the algorithm  $\mathcal{A}$  to obtain a depth map and a segmentation mask. We then do occlusion checking with the given image to exclude pixels that are definitely occluded (based on a threshold  $t_{occlusion}$ ). This gives us the visible part of the object  $P_{visible}$ . We then compute the intersection  $I$  between the output and the ground truth  $G$  by counting the number of pixels which are contained in both  $P_{visible}$  and  $G$ , but in addition also agree on their depth values by being within a distance threshold of  $t_{agree}$  with each other. Union  $U$  is computed by counting the number of pixels in the ground truth  $G$  and the visible extent of the object  $P_{visible}$  as  $|G \cup P_{visible}|$ . If this  $\frac{I}{U}$ , is larger than  $t_{iou}$  then this prediction is considered to explain the data well, otherwise not. With this modified definition of overlap, we plot a precision recall curve and measure the area under it as measure of the performance of the algorithm  $\mathcal{A}$ . We denote this average precision as  $AP^m$ . To account for the inherent noise in the sensor we operate with disparity as opposed to the depth value, and set thresholds  $t_{occluded}$  and  $t_{agree}$  on disparity. Doing this allows for larger error in far away objects as opposed to close by objects. While this behavior may not be desirable, it is unavoidable given the noise in the input depth image behaves similarly.

**Evaluation** We evaluate our algorithm in 3 different settings: first using ground truth segmentations, second using high scoring instance segmentations from Gupta et al. [13] that overlap with the ground truth by more than 50% (denoted as ‘latent positive setting’), and third a completely unconstrained setting using only the instance segmentation

**Table 3: Control experiments for model placement on NYUD2 *val* set:** We report the  $AP^m$  for the three different setting we tested our algorithm on: using ground truth object segmentation masks, using latent positive segmentation masks and using the detection output from the instance segmentation from [13]. We report performance on two different values for threshold  $t_{agree}$ . See Section 5.2.3 for details.

|             | ground truth segm |             | latent positive setting |             |             | detection setting |             |             |
|-------------|-------------------|-------------|-------------------------|-------------|-------------|-------------------|-------------|-------------|
|             | 0.5, 5            | 0.5, 5      | 0.5, 5                  | 0.5, 5      | $AP^r$      | 0.5, 5            | 0.5, 5      | $AP^r$      |
| $t_{agree}$ | 7                 | $\infty$    | 7                       | $\infty$    | upper bound | 7                 | $\infty$    | upper bound |
| bathtub     | 57.4              | 76.8        | 55.3                    | 83.3        | 94.7        | 6.7               | 19.4        | 25.7        |
| bed         | 42.3              | 87.3        | 28.8                    | 86.0        | 96.1        | 25.8              | 63.2        | 57.0        |
| chair       | 45.3              | 74.1        | 29.0                    | 56.9        | 70.1        | 11.8              | 25.2        | 30.4        |
| desk        | 33.9              | 67.4        | 20.3                    | 40.9        | 55.7        | 3.0               | 4.0         | 6.2         |
| dresser     | 82.7              | 92.0        | 76.1                    | 96.0        | 100.0       | 13.3              | 21.1        | 21.1        |
| monitor     | 31.4              | 39.8        | 18.4                    | 20.8        | 41.3        | 12.5              | 12.5        | 26.8        |
| night-stand | 62.5              | 77.6        | 51.3                    | 65.2        | 87.9        | 18.9              | 21.6        | 25.5        |
| sofa        | 45.1              | 85.0        | 28.5                    | 72.0        | 92.4        | 10.5              | 30.4        | 37.7        |
| table       | 18.8              | 52.2        | 15.8                    | 34.3        | 46.8        | 5.5               | 11.9        | 13.3        |
| toilet      | 66.0              | 100.0       | 46.0                    | 86.0        | 100.0       | 35.9              | 72.4        | 73.2        |
| <b>mean</b> | <b>48.5</b>       | <b>75.2</b> | <b>37.0</b>             | <b>64.1</b> | <b>78.5</b> | <b>14.4</b>       | <b>28.2</b> | <b>31.7</b> |

**Table 4: Results for model placement on NYUD2 *test* set:** We report the  $AP^m$  in the detection setting. See Section 5.2.3 for details.

|             | detection setting |             |             |
|-------------|-------------------|-------------|-------------|
|             | 0.5, 5            | 0.5, 5      | $AP^r$      |
| $t_{agree}$ | 7                 | $\infty$    | upper bound |
| bathtub     | 7.9               | 50.4        | 42.0        |
| bed         | 31.8              | 68.7        | 65.0        |
| chair       | 14.7              | 35.6        | 42.9        |
| desk        | 4.1               | 10.8        | 12.0        |
| dresser     | 26.3              | 35.0        | 36.1        |
| monitor     | 5.7               | 7.4         | 11.4        |
| night-stand | 28.1              | 33.7        | 34.8        |
| sofa        | 21.8              | 48.5        | 47.4        |
| table       | 5.6               | 12.3        | 15.0        |
| toilet      | 41.8              | 68.4        | 68.4        |
| <b>mean</b> | <b>18.8</b>       | <b>37.1</b> | <b>37.5</b> |

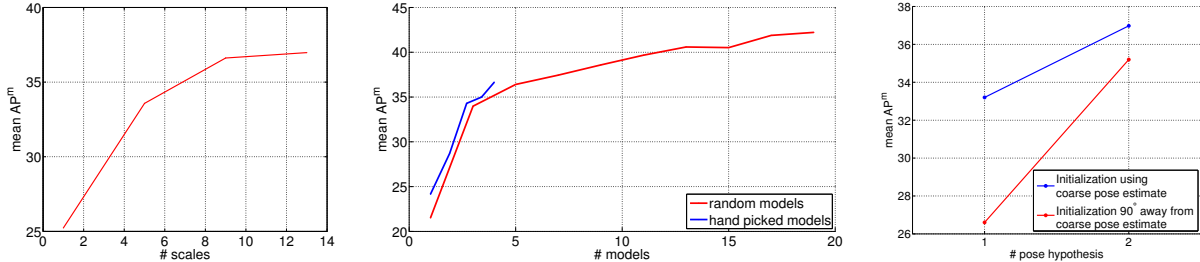


**Figure 6: Control Experiment:** Variation in  $AP^m$  as we change number of scales, number of models and number of pose hypothesis we search over in our model alignment stage.

output without any ground truth (denoted as ‘detection setting’). Table 3 summarizes results in these settings on the *val* set.

We use an  $t_{iou}$  of 0.5 to count a true positive,  $t_{occlusion}$  of 5 disparity units, and report performance at two different values of  $t_{agree}$  7 and  $\infty$ . An error of 7 disparity units corresponds to a 20 cm error at 3 meters. A  $t_{agree}$  of  $\infty$  corresponds to  $AP^r$  subject to the constraint that the segmentation must come from the rendering of a 3D model.

We see that even when working with ground truth segmentations, estimating and placing a 3D model to explain the segment is a hard task. We obtain a (model average precision)  $AP^m$  of 48.5% in this setting. Even when evaluating at  $t_{agree}$  of  $\infty$ , we only get a performance of 75.2%

which is indicative of the variety of our 3D model library and accuracy of our pose estimator.

In the second setting, we take the highest scoring detection which overlaps with more than 50% with the ground truth mask. Note that this setup decouples the performance of the detector from the performance of the model placement algorithm while at the same time exposing the model placement algorithm with noisier segmentation masks. Under this setting, the  $AP^r$  upper bound is 78.5% which means that only as many percentage of regions have a bottom-up region which overlaps with more than 0.5 with the ground truth mask, indicating the recall of the region proposal generator that we are using [13]. In this setting the performance at  $t_{agree} = \infty$  is 64.1% and at  $t_{agree} = 7$  is

37.0%. This shows that our model alignment is fairly robust to segmentation errors and we only see a small drop in performance from 48.5% to 37.0% when moving from ground truth setting to latent positive setting.

In the setting when we work with detections (using no ground truth information at all), we observe a  $AP^r$  upper bound of 31.7% (which are comparable to  $AP^r$  reported in Table 1 but slightly different because a) we ignore pixels with missing depth values in computing this metric and b) these are on the validation set). In this setting we observe a performance of 14.4% for  $t_{agree}$  of 7 and 28.2% for  $t_{agree}$  of  $\infty$ . We also report  $AP^m$  on the *test* set in the detection setting in Table 4.

**Control Experiments** We do additional control experiments to study the affect of the number of scales, the number of models, difference in hand picking models versus randomly picking models, number of pose hypothesis, and the importance of initialization for the model alignment stage. These experiments are summarized in Figure 6 and discussed below.

As expected, performance improves as we search over more scales (but saturates around 10 scales) (Figure 6 left). The performance increases as we use more models. Hand picking models so that they capture different modes of variation is better than picking models randomly, and that performance does not seem to saturate as we keep increasing the number of models we use during model alignment step (Figure 6 center), although this comes at proportionately larger computation time. Finally, using two pose hypothesis is better than using a single hypothesis. The model alignment stage is indeed sensitive to initialization and works better when used with the pose estimate from Section 3. This difference is more pronounced when using a single pose hypothesis (33% using our pose estimate versus 27% when not using it, Figure 6 right).

**Qualitative Visualizations** Finally, we provide qualitative visualizations of the output of our method in Figure 7 for chair, bed, sofa, and toilets categories. We also show images where multiple objects have been replaced with 3D models in Figure 8.

**Acknowledgements:** The authors would like to thank Shubham Tulsiani for his valuable comments. This work was supported by ONR SMARTS MURI N00014-09-1-1051, ONR MURI N00014-10-10933, and a Berkeley Graduate Fellowship. We gratefully acknowledge NVIDIA corporation for the donation of Tesla and Titan GPUs used for this research.

## References

- [1] P. Arbeláez, B. Hariharan, C. Gu, S. Gupta, L. Bourdev, and J. Malik. Semantic segmentation using regions and parts. In *CVPR*, 2012. [2](#)
- [2] M. Aubry, D. Maturana, A. Efros, B. Russell, and J. Sivic. Seeing 3d chairs: exemplar part-based 2d-3d alignment using a large dataset of cad models. In *CVPR*, 2014. [2](#)
- [3] D. Banica and C. Sminchisescu. CPMC-3D-O2P: Semantic segmentation of RGB-D images using CPMC and second order pooling. *CoRR*, abs/1312.7715, 2013. [2](#)
- [4] L. Bo, X. Ren, and D. Fox. Learning hierarchical sparse features for rgb-(d) object recognition. *The International Journal of Robotics Research*, 33(4):581–599, 2014. [2](#)
- [5] J. Carreira, R. Caseiro, J. Batista, and C. Sminchisescu. Semantic segmentation with second-order pooling. In *ECCV*, 2012. [2](#)
- [6] N. Dalal and B. Triggs. Histograms of oriented gradients for human detection. In *CVPR*, 2005. [2](#)
- [7] P. Felzenszwalb, R. Girshick, D. McAllester, and D. Ramanan. Object detection with discriminatively trained part based models. *TPAMI*, 2010. [2](#)
- [8] R. Girshick, J. Donahue, T. Darrell, and J. Malik. Rich feature hierarchies for accurate object detection and semantic segmentation. In *CVPR*, 2014. [2, 3](#)
- [9] R. Guo and D. Hoiem. Support surface prediction in indoor scenes. In *ICCV*, 2013. [2, 3, 5](#)
- [10] R. Guo and D. Hoiem. *Scene understanding with complete scenes and structured representations*. PhD thesis, UIUC, 2014. [2, 5, 8](#)
- [11] S. Gupta, P. Arbeláez, R. Girshick, and J. Malik. Indoor scene understanding with RGB-D images: Bottom-up segmentation, object detection and semantic segmentation. *IJCV*, 2014. [2](#)
- [12] S. Gupta, P. Arbeláez, and J. Malik. Perceptual organization and recognition of indoor scenes from RGB-D images. In *CVPR*, 2013. [2, 3, 4](#)
- [13] S. Gupta, R. Girshick, P. Arbeláez, and J. Malik. Learning rich features from RGB-D images for object detection and segmentation. In *ECCV*, 2014. [1, 2, 3, 5, 6, 7, 8, 9](#)
- [14] B. Hariharan, P. Arbeláez, R. Girshick, and J. Malik. Simultaneous detection and segmentation. In *ECCV*, 2014. [2, 6, 7, 8](#)
- [15] V. Hedau, D. Hoiem, and D. Forsyth. Thinking inside the box: Using appearance models and context based on room geometry. In *ECCV*, pages 224–237. Springer, 2010. [2](#)
- [16] M. Hejrati and D. Ramanan. Analyzing 3d objects in cluttered images. In *Advances in Neural Information Processing Systems*, pages 593–601, 2012. [2](#)
- [17] A. Janoch, S. Karayev, Y. Jia, J. T. Barron, M. Fritz, K. Saenko, and T. Darrell. A category-level 3D object dataset: Putting the kinect to work. In *Consumer Depth Cameras for Computer Vision*. 2013. [2](#)
- [18] H. Koppula, A. Anand, T. Joachims, and A. Saxena. Semantic labeling of 3d point clouds for indoor scenes. In *NIPS*, 2011. [2](#)

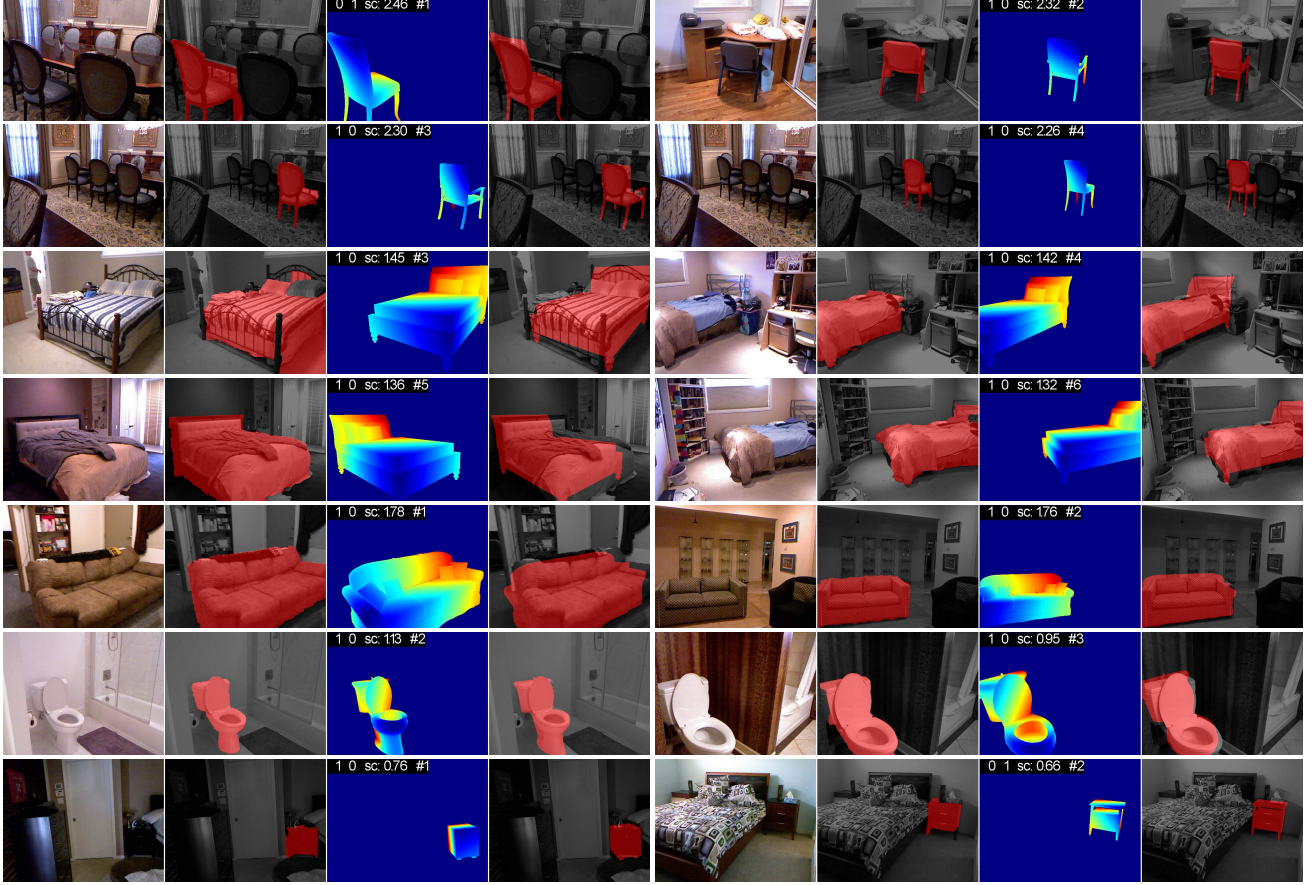
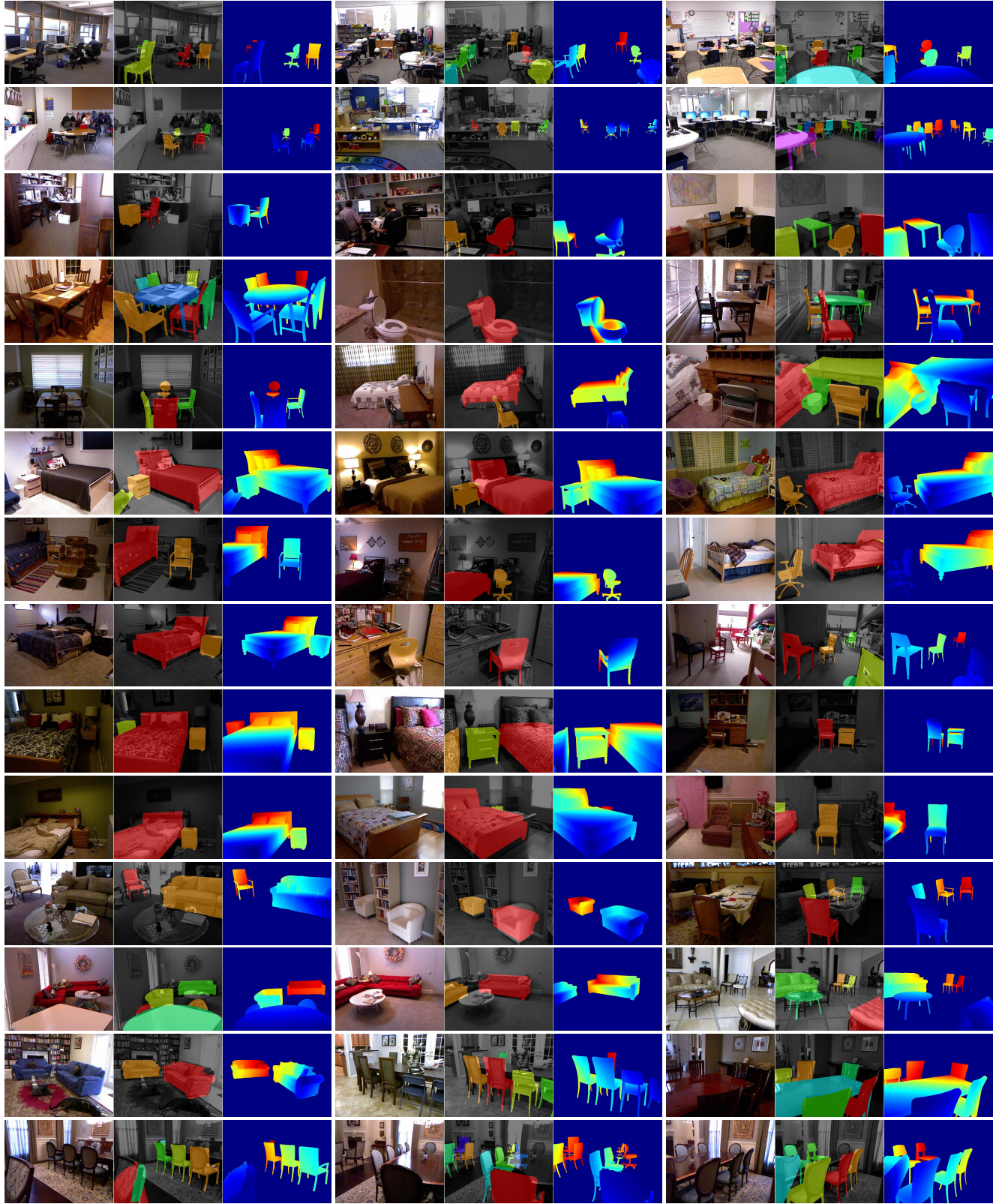


Figure 7: **Visualizations of the output on the *test* set:** We show instance segmentation mask, rendered model, and rendered model overlaid on image for high scoring detections for chairs, beds, sofas, toilets and night-stands.

- [19] K. Lai, L. Bo, and D. Fox. Unsupervised feature learning for 3d scene labeling. In *IEEE International Conference on on Robotics and Automation*, 2014. [2](#)
- [20] K. Lai, L. Bo, X. Ren, and D. Fox. A large-scale hierarchical multi-view rgbd object dataset. In *ICRA*, 2011. [2](#)
- [21] K. Lai, L. Bo, X. Ren, and D. Fox. Detection-based object labeling in 3D scenes. In *IEEE International Conference on on Robotics and Automation*, 2012. [2](#)
- [22] J. J. Lim, A. Khosla, and A. Torralba. Fpm: Fine pose parts-based model with 3d cad models. In *Computer Vision–ECCV 2014*, pages 478–493. Springer International Publishing, 2014. [2](#)
- [23] D. Lin, S. Fidler, and R. Urtasun. Holistic scene understanding for 3D object detection with RGBD cameras. In *ICCV*, 2013. [2](#)
- [24] X. Ren, L. Bo, and D. Fox. RGB-(D) scene labeling: Features and algorithms. In *CVPR*, 2012. [2](#)
- [25] H. Rowley, S. Baluja, and T. Kanade. Human face detection in visual scenes. Technical Report CMU-CS-95-158R, Carnegie Mellon University, 1995. [2](#)
- [26] S. Rusinkiewicz and M. Levoy. Efficient variants of the icp algorithm. In *3-D Digital Imaging and Modeling*, 2001. [2](#)
- [Proceedings. *Third International Conference on*, pages 145–152. IEEE, 2001. [4](#)
- [27] R. F. Salas-Moreno, R. A. Newcombe, H. Strasdat, P. H. Kelly, and A. J. Davison. Slam++: Simultaneous localisation and mapping at the level of objects. In *CVPR*, 2013. [2](#)
- [28] S. Satkin, M. Rashid, J. Lin, and M. Hebert. 3dnn: 3d nearest neighbor. *IJCV*, pages 1–29, 2014. [2](#)
- [29] A. G. Schwing, S. Fidler, M. Pollefeys, and R. Urtasun. Box in the box: Joint 3D layout and object reasoning from single images. In *ICCV*, 2013. [2](#)
- [30] T. Shao, W. Xu, K. Zhou, J. Wang, D. Li, and B. Guo. An interactive approach to semantic modeling of indoor scenes with an rgbd camera. *ACM Transactions on Graphics (TOG)*, 31(6):136, 2012. [2](#)
- [31] N. Silberman, D. Hoiem, P. Kohli, and R. Fergus. Indoor segmentation and support inference from RGBD images. In *ECCV*, 2012. [2, 3, 4, 8](#)
- [32] N. Silberman, D. Sontag, and R. Fergus. Instance segmentation of indoor scenes using a coverage loss. In *ECCV*, 2014. [2](#)
- [33] S. Song and J. Xiao. Sliding shapes for 3D object detection in depth images. In *ECCV*. Springer, 2014. [1, 2, 5, 6, 7, 8](#)



**Figure 8: Visualizations of the output on the *test* set:** We show images with multiple objects replaced with corresponding 3D CAD models. We show the image, models overlaid onto the image and the depth map for models placed in the scene. Depth maps are visualized using the ‘jet’ colormap, far away points are red and and close by points are blue.

- [34] B. soo Kim, S. Xu, and S. Savarese. Accurate localization of 3D objects from RGB-D data using segmentation hypotheses. In *CVPR*, 2013. [2](#)
- [35] S. Tang, X. Wang, X. Lv, T. X. Han, J. Keller, Z. He, M. Skubic, and S. Lao. Histogram of oriented normal vectors for object recognition with a depth sensor. In *ACCV*, 2012. [2](#)
- [36] J. Tighe, M. Niethammer, and S. Lazebnik. Scene parsing with object instances and occlusion ordering. In *CVPR*, 2014. [2](#)
- [37] P. Viola and M. Jones. Rapid object detection using a boosted cascade of simple features. In *CVPR*, 2001. [2](#)
- [38] Z. Wu, S. Song, A. Khosla, X. Tang, and J. Xiao. 3D shapenets for 2.5D object recognition and next-best-view prediction. *CoRR*, abs/1406.5670, 2014. [3](#), [4](#), [5](#)
- [39] M. Z. Zia, M. Stark, B. Schiele, and K. Schindler. Detailed 3D representations for object recognition and modeling. *TPAMI*, 2013. [2](#)